Available online at www.sciencedirect.com
SCIENCE DIRECT
Geochimica et Cosmochimica Acta 70 (2006) 516–531
Geochimica
www.elsevier.com/locate/gca

Graves Nunataks 95209: A snapshot of metal segregation and core formation

T.J. McCoy [a,*], W.D. Carlson [b], L.R. Nittler [c], R.M. Stroud [d], D.D. Bogard [e], D.H. Garrison [e]

[a] Department of Mineral Sciences, National Museum of Natural History, Smithsonian Institution, Washington, DC 20560-0119, USA
[b] Department of Geological Sciences, University of Texas at Austin, Austin, TX 78712, USA
[c] Department of Terrestrial Magnetism, Carnegie Institution of Washington, 5241 Broad Branch Rd NW, Washington, DC 20015, USA
[d] Code 6361, Naval Research Laboratory, Washington, DC 20375, USA
[e] ARES, Code KA, NASA/Johnson Space Center, Houston, TX 77058, USA

Received 26 April 2005; accepted in revised form 6 September 2005

Abstract

GRA 95209 may provide our best opportunity to date to understand the earliest stages of core formation in asteroidal bodies. This lodranite preserves a physically, chemically, and mineralogically complex set of metal–sulfide veins. High-resolution X-ray computed tomography revealed three distinct lithologies. The dominant mixed metal–silicate–sulfide matrix is cut by metal-rich, graphite-bearing veins exceeding 1 cm in width and grades into a volumetrically minor metal-poor region. Silicate compositions and modal abundances are typical for lodranites, while the mineralogy of the metal–sulfide component is complex and differs among the three lithologies. Kamacite and troilite occur with chromite, tetrataenite, schreibersite, graphite, and a range of phosphates. An ^{39}Ar–^{40}Ar age of 4.521 ± 0.006 Ga measures the time of closure of the K–Ar system. Carbon rosettes within the metal-rich vein are nitrogen-poor, well crystallized, include kamacite sub-grains of composition comparable to the host metal, and are essentially isotopically homogeneous ($\delta^{13}C \sim -33‰$). In contrast, carbon rosettes within metal of the metal-poor lithology are N-poor, poorly crystallized, include kamacite grains that are Ni-poor compared to their host metal, and are isotopically heterogeneous ($\delta^{13}C$ ranging from -50 to $+80‰$) even within a single metal grain. The silicate portion of GRA 95209 is similar to the lodranite EET 84302, sharing a common texture, silicate mineral compositions, and Ar–Ar age. GRA 95209 and EET 84302 are intermediate between acapulcoites and lodranites. Both experienced Fe,Ni-FeS melting with extensive melt migration, but record only the onset of silicate partial melting with limited migration of silicate melt. The complex metal–sulfide veins in GRA 95209 resulted from low-degree partial melting and melt migration and intruded the matrix lithology. Reactions between solid minerals and melt, including oxidation–reduction reactions, produced the array of phosphates, schreibersite, and tetrataenite. Extensive reduction in the metal-rich vein resulted from its origin in a hotter portion of the asteroid. This difference in thermal history is supported by the graphite structures and isotopic compositions. The graphite rosettes in the metal-rich vein are consistent with high-temperature igneous processing. In contrast, the carbon in the metal-poor lithology appears to preserve a record of formation in the nebula prior to parent-body formation. Carbon incorporated from the solar nebula into a differentiating asteroid is preferentially incorporated in metal–sulfide melts that form a core, but does not achieve isotopic homogeneity until extensive thermal processing occurs.

1. Introduction

Meteorites testify to the extreme range of heating of asteroids, from those that experienced only mild metamorphism to parent bodies that experienced complete melting and differentiation at temperatures in excess of 1600 °C (Mittlefehldt et al., 1998). The diversity and numbers of igneous meteorites suggest that the majority of sampled asteroids (~105 of 135 or ~80%; Meibom and Clark, 1999) experienced some degree of melting and differentiation. The vast majority of these asteroids are represented by iron meteorites from both the major groups and the ~70 parent bodies represented by the ~120 ungrouped iron

* Corresponding author.
E-mail address: mccoy.tim@nmnh.si.edu (T.J. McCoy).

0016-7037/$ - see front matter © 2005 Elsevier Inc. All rights reserved.
doi:10.1016/j.gca.2005.09.019

meteorites (Wasson, 1995). This predominance of irons further suggests that most asteroids that experienced any melting were subjected to extensive melting, metal segregation, and core formation.

In contrast to the apparent importance of core formation as a geologic process in shaping asteroids, it remains a process that is poorly understood. Experimental studies (Rushmer et al., 2000, and references therein) have contributed to our understanding of the mechanisms by which primitive, chondritic asteroids are transformed into layered, differentiated worlds. Yet, in large part, our ignorance of the chemical and physical processes that form metallic cores results from the lack of meteorites that capture the early stages of metal segregation. This situation appears to be changing with the discovery of meteorites that experienced limited degrees of partial melting and melt migration, sometimes capturing this process frozen in time. Among the suite of acapulcoites and lodranites, Monument Draw preserves metal–sulfide–phosphate veins (McCoy et al., 1996) and Lewis Cliffs 86220 preserves metal–sulfide–gabbro melts inside an acapulcoite host (McCoy et al., 1997b). Unfortunately, the amount of material available for study from these two meteorites is extremely limited. The discovery of the lodranite Graves Nunataks (GRA) 95209 and the metal veins it preserves offers the opportunity to shed new light on the early stages of metal segregation leading to core formation.

2. Macroscopic description and X-ray computed tomography

The metal in GRA 95209 is very heterogeneously distributed, as was discovered during the initial description and allocation of this meteorite. The original 948.8 g flight-oriented mass of the meteorite was initially broken, with several pieces totaling ~240 g removed from the main mass. In the description of these pieces, McBride and Mason (1997) noted the abundance of metal grains, including areas of concentrated metal up to 1 cm in diameter. The meteorite was classified as a lodranite and mineral compositions within the range of typical lodranites (olivine, Fa_7; orthopyroxene, Fs_7) were noted. Several features that would be highly unusual for lodranites (e.g., chondrules, clasts) were also noted, prompting McBride and McCoy (1997) to revisit the hand-sample description. By this time, an ~1 cm thick slice of ~130 g had been cut from the main mass. Rather than revealing an expected vein-like structure in the meteorite, the cutting revealed an area of metal 2 by 3 cm on a side adjacent to the fusion crust (Fig. 1A). Coupled with this observation was the presence of a series of ablation pits on the fusion crust which McBride and McCoy (1997) thought might outline a very large (~20% of the mass) metal particle on the flight-oriented exterior surface. Areas described by McBride and Mason (1997) were not clasts in the traditional sense (fragments of other rocks), but areas relatively depleted in metal. Realizing the complexity of the metal distribution within GRA 95209, we undertook an X-ray computed tomography study of the remaining mass (554 g).

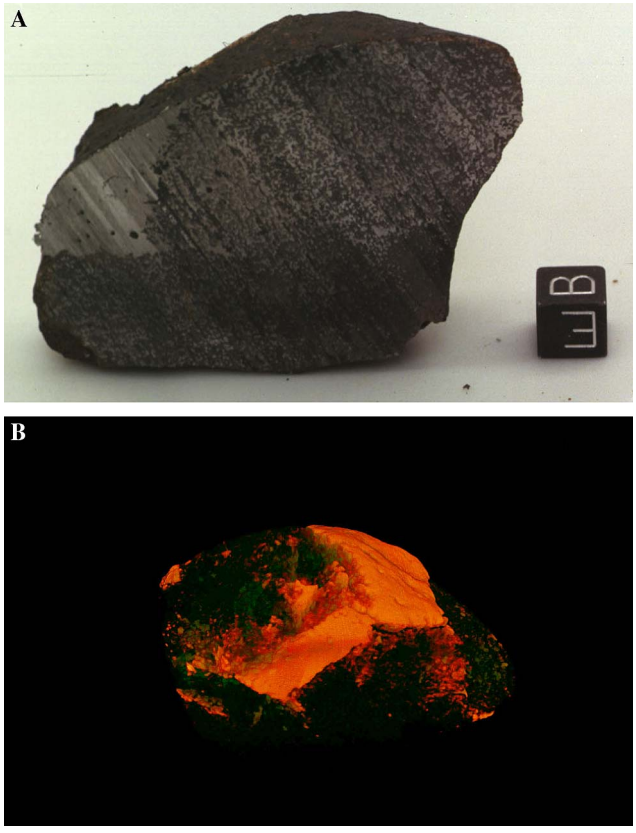

Fig. 1. Images of the 554 g mass of GRA 95209 used for CT scanning. (A) Photograph (NASA JSC #S97-07949) of the cut face of this mass showing the large metal mass with small, round graphite rosettes. Scale cube is 1 cm on a side. Apparent difference in metal abundance within the matrix between the upper and lower half is a lighting artifact. (B) Three-dimensional representation of computed tomography data of this mass showing that the triangular area of metal on the cut face is connected to a large sheet of metal (orange) which caps and intrudes silicates (semi-transparent blue). In this image, the specimen has been rotated relative to (A), bringing the top surface towards the reader and down, and tilting the specimen to the right. This image is the last frame in a rotational movie that can be viewed at http://www.ctlab.geo.utexas.edu/pubs/mccoy_et_al/mccoy_et_al.htm.

Images revealing the internal distribution and modal proportions of lithologic types in the 554 g mass of GRA 95209 were obtained at the high-resolution X-ray computed tomography (CT) facility of the University of Texas at Austin. To prevent contamination, the meteorite processing laboratory at NASA/JSC first sealed the specimen in two nylon bags. At the University of Texas CT facility, it was then surrounded by finely powdered iron in a plastic cylinder to reduce beam-hardening artifacts during scanning (cf. Ketcham and Carlson, 2001). An unfiltered tungsten X-ray source operating at 420 kV and 5 mA was used to acquire 320 two-dimensional CT images (“slices”) perpendicular to the existing saw cut on the specimen, each constructed from 3600 views, resulting in a scan time of approximately 8 min per slice. Each of these slices illuminated a 250-μm-thick planar slab in the specimen. Spacing the slices 250 μm apart yielded a contiguous set of images that were integrated into a complete three-dimensional

data volume. Because the 72-mm-diameter field of view was reconstructed on a 512×512 matrix, the size of each voxel in the three-dimensional data set is approximately $140 \times 140 \times 250$ μm. These data can be displayed in a number of ways: as the individual CT images (“slices”); as Quick Time movies of the “slices” in sequence (a “flipbook”); as a Quick Time movie of a three-dimensional representation that can be rotated in two dimensions; and as reconstructed “slices” parallel to the existing saw cut of the specimen (“virtual saw cuts”). These images can be viewed at http://www.ctlab.geo.utexas.edu/pubs/mccoy_et_al/mccoy_et_al.htm. We utilized each of these formats in examining this data set.

The CT images revealed three major lithologic types that were hinted at in the macroscopic descriptions and sampled for petrographic studies (discussed below). These types are the prominent metal veins, the metal-poor regions, and the matrix that serves as the host for the other two lithologies and is the dominant lithology in GRA 95209. CT contrast is produced by differences within an object in the linear attenuation coefficients for the X-ray spectrum used (cf. Ketcham and Carlson, 2001); these differences correlate strongly with differences in mass density. In CT imagery, brighter grayscale values are conventionally assigned to voxels with stronger attenuation. As a result, metal veins are prominent in the images as homogeneous bright regions. The matrix hosting the veins appears as a darker but mottled region, reflecting the intermingling of individual metal and silicate particles at a scale close to the limit of spatial resolution of the images. Because of partial volume effects, voxels containing metal particles with sizes below the limit of spatial resolution take on grayscale levels lower than those for metal in veins (cf. Ketcham and Carlson, 2001); this allows discrimination between veins and matrix when making quantitative determinations of modal proportions. The metal-poor lithology appears in the CT imagery as still darker, slightly mottled regions.

The three-dimensional CT data reveal that the $\sim 3 \times 2$ cm area of metal visible on the sawn surface of the specimen is part of a large ‘slab’ of metal ~6–12 mm thick, present along the exterior surface of much of the specimen and extending into its interior (Figs. 1B and 2A). This slab of metal is connected to several narrow (~0.5–4 mm wide) veins and stringers of metal in the specimen’s interior (Figs. 2A and D). Within the metal slab are numerous rounded, equant globules of very low-density material, commonly up to ~3 mm in diameter, identified by reflected-light petrography as carbon-rich rosettes (Fig. 2B). Through much of this paper, we term these rosettes “graphite,” although we show later that much of the elemental carbon in GRA95209, especially within the metal-poor lithology, is better described as “poorly graphitized carbon” rather than “graphite.” The matrix of intermingled silicates and metal abuts the thick metal slab across an interface that is sharp and smooth along much of its length, but locally gradational (Fig. 2B). The metal-poor regions are in contact with the matrix across interfaces that are gradational over distances of a few grain diameters (Fig. 2C).

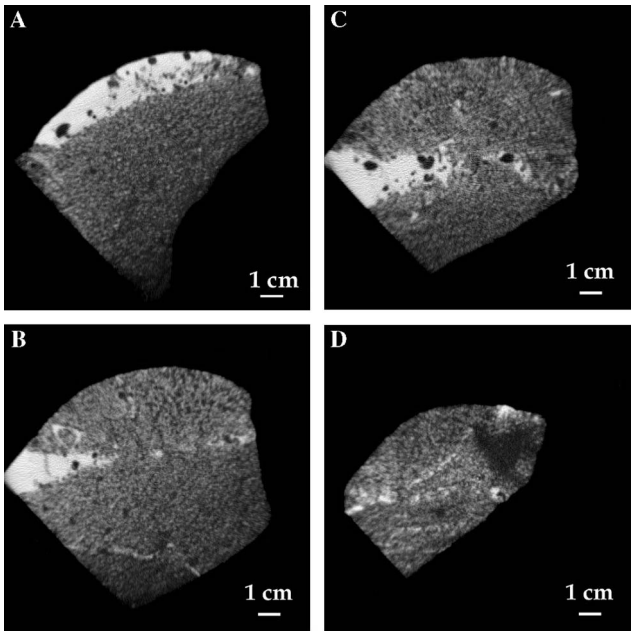

Fig. 2. Individual CT images (“slices”) through the 554 g mass of GRA 95209. These slices are frames in a flipbook movie that can be viewed at http://www.ctlab.geo.utexas.edu/pubs/mccoy_et_al/mccoy_et_al.htm. In each, the linear boundary at the left is the intersection of the sawn surface with the image plane. Brightness corresponds roughly with metal abundance. Very dark areas within the metal veins are graphite rosettes. (A) Much of the flight-oriented surface of the meteorite is capped by a metal sheet containing abundant graphite rosettes. (B) Metal veins and veinlets exhibit a range of sizes. Apparently disconnected metal blebs extending to the right from the main metal mass are in fact connected to it in the third dimension. Note the delicate veinlet at the bottom, which connects with the larger metal vein in three dimensions. (C) In places, the metal vein exhibits delicate interfingering of metal with matrix (mottled gray areas), and numerous inclusions of graphite within metal. (D) The largest metal-deficient zone (dark, slightly mottled region at right) is found at one end of the meteorite, but well inside the specimen. Note the distinct but gradational interfaces with matrix, and intersection of two narrow veinlets.

Modal proportions of the three lithologic types and the graphite rosettes were determined from quantitative analysis of the two-dimensional CT data using NIH Image software. Metal veins and their included graphite rosettes were segregated on the basis of their high and low grayscale values; metal-poor regions were outlined manually in each slice and the number of pixels in each such area were automatically counted; and the matrix volume was determined by difference. The volumetric modal proportions determined in this manner are: metal veins 6.4%, graphite rosettes 0.3%, metal-poor regions 1.9%, and matrix 91.4%.

The computed tomography data were recast as “virtual saw cuts” to select material for additional studies. One of these virtual saw cuts ~13 mm into the specimen (Fig. 3B) and parallel to the existing cut indicated the presence of all three types of materials (matrix, metal-depleted region, and metal-rich vein). Further, large graphite

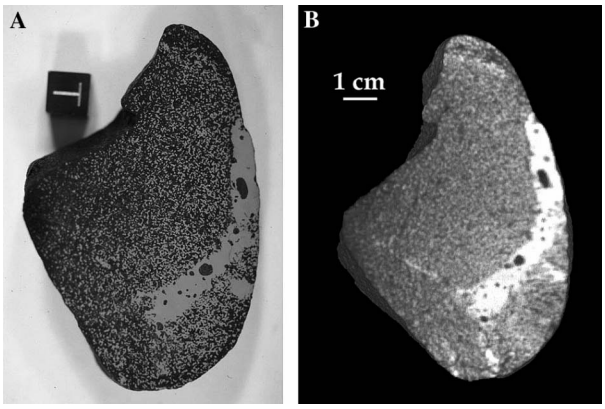

Fig. 3. Actual and virtual saw cuts of GRA 95209 taken ~13 mm from the first saw cut. (A) The slice shows a prominent metal vein extending into the interior, surrounded by matrix material and with a metal-deficient region at the anterior point. Large graphite rosettes are present in the metal. (B) The virtual saw cut was reconstructed from CT scans and served as a guide to locating the ideal place to cut to obtain the most representative sample.

rosettes were indicated within the metal vein and the metal vein extended well into the interior of the specimen, away from the heat-altered zone formed during atmospheric passage. We cut the specimen at this ~13 mm depth, producing the polished slab illustrated in Fig. 3A. The striking similarity between the "virtual" and real saw cuts confirms the utility of computed tomography as a curatorial tool for valuable, complex specimens.

3. Petrology

We examined nine polished sections or polished thin sections in our study. Polished thin sections 7 and 9 were from the initial chip used for classification by McBride and Mason (1997) and sample the "matrix" lithology of intermixed metal and silicates. The next set of sections studied were PTSs 40 and 43 of the matrix lithology, PTS 42 of the metal-poor region, and polished section (PS) 223 of the metal-rich sheet (McBride and McCoy, 1997). From the last slab cut from the main mass (the surface imaged by the computed tomography virtual saw cut), we examined PSs 150 and 170 from the metal-rich sheet. PS 150 was from the deepest interior extension of the metal-rich sheet, while PS 170 was taken from the surface and included the heat-altered zone of the meteorite. We also examined PTS 210 taken from the metal-poor region of the final slab.

Polished sections were studied optically in both transmitted and reflected light. All mineral analyses were conducted using a JEOL JXA-8900R electron microprobe using a fully focused beam, 15 kV accelerating voltage and 20 nA beam current. Well-known mineral standards were used and the data were corrected with manufacturer-supplied ZAF routines. Suitable standards for the full range of phosphate compositions found in GRA 95209 were not available. The selected standards yielded somewhat high totals for the magnesian phosphate farringtonite. Mineral mapping was conducted using a JEOL scanning electron microscope. Back-scattered electron images and co-registered elemental maps were used to determine the distribution of silicate and opaque phases within this meteorite. The base map (olivine, orthopyroxene, clinopyroxene, and plagioclase) was produced by combining X-ray maps of Si, Mg and Ca. Additional X-ray maps were used to map kamacite (Fe), troilite (S), and phosphate (P). Graphite yielded no signal in the X-ray maps and large graphite rosettes were identified optically. Modal abundances were determined using pixel-counting of false-color mosaics in Photoshop.

Silicates occur as intimately mixed grains 50 μm to 2 mm in long dimension with average grain sizes of 200–400 μm. Textures and mineral distributions are illustrated in Figs. 4 and 5. Mittlefehldt and Lindstrom (1998) suggested that GRA 95209 was texturally heterogeneous, with finer-grained regions resembling acapulcoites and coarser-grained regions similar to lodranites. Textural variations within the matrix lithology are limited to regions ~0.5 mm across and fine- and coarse-grained regions grade into each other over distances of 1–2 mm. We do note that the metal-poor lithology appears somewhat finer-grained than the matrix lithology, probably owing to a decrease in the number of larger olivine and pyroxene grains. Overall, the texture is equigranular with abundant 120° triple junctions and is quite similar to EET 84302, which is transitional between acapulcoites and lodranites (Mittlefehldt et al., 1996; McCoy et al., 1997a,b). Olivine grains exhibit sharp extinction consistent with shock stage S1 (Stöffler et al., 1991). Metal often exhibits rims of hydrated iron oxides produced by terrestrial weathering.

Mineral distributions and abundances in GRA 95209 vary dramatically among the lithologies (Fig. 5, Table 1). It should be noted that the mode given for the metal-rich sheet is for an entire polished section of which only a portion is the metal-rich sheet. It is not surprising that metal abundances vary so greatly among lithologies, given that this was the primary distinguishing characteristic. Olivine:orthopyroxene ratios (ol/(ol + opx) of 50.5–61.9) also vary significantly on a scale of 2–3 mm, and this is particularly evident in the metal-poor lithology of GRA 95209 (Fig. 5B). Feldspar abundances are similar (9.6–16.6% of total silicates in GRA 95209) to those in H chondrites (12.8%; McSween et al., 1991). GRA 95209 is markedly depleted in troilite relative to metal (troilite/(troilite + metal) = 0.4–13.5%).

We measured compositions of olivine, pyroxene, and plagioclase from the matrix, metal-poor area, and metal-rich sheet (Table 2) as a test for heterogeneity. Olivine in all three lithologies has a composition of $Fa_{7.3\pm0.2}$. Low-Ca pyroxene has a composition of $Fs_{7.3\pm0.2}Wo_{3.2\pm0.2}$ and high-Ca pyroxene is $Fs_{3.6\pm0.3}Wo_{42.8\pm0.4}$, with no difference observed between the various lithologies. Plagioclase compositions are essentially identical among the three lithologies ($An_{17.5\pm0.6}Or_{2.0\pm0.5}$). The silicate compositions are similar to those reported by Mittlefehldt and Lindstrom

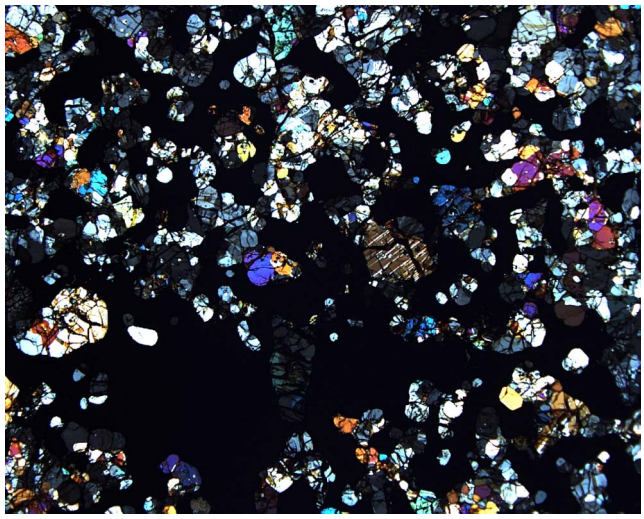

Fig. 4. Transmitted light photomicrograph of the matrix lithology of GRA 95209 (PTS, 40) illustrating local variability in this medium-grained member of the acapulcoite–lodranite clan. Field of view is 7 mm.

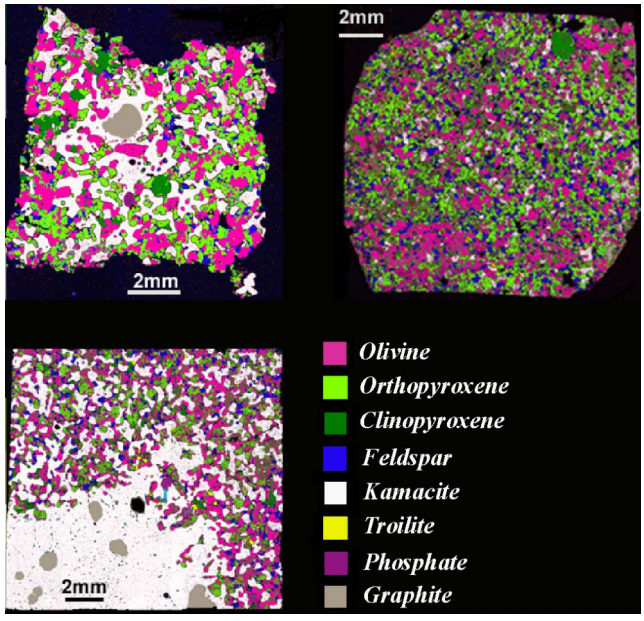

Fig. 5. Maps of mineral distributions in thin sections of the three lithologies of GRA 95209. Upper left is the matrix lithology (PTS, 40) with a single large graphite rosette within metal, phosphates both as large agglomerates (of the type studied by Floss (1999)) and rimming kamacite, large clinopyroxene grains, and equigranular silicates. The metal-poor region (upper right) (PTS, 210) is finer-grained overall and may contain an olivine-rich area. The metal-rich sheet (PTS, 150) is sampled in the lower right portion of this section and exhibits numerous large graphite rosettes.

(1998). Olivine and orthopyroxene in GRA 95209 are similar to compositions for EET 84302 ($Fa_{8.4}$, $Fs_{8.3}$), providing yet another link between these two meteorites.

Unlike the silicates, the opaque minerals and associated phases differ substantially among the various lithologies of GRA 95209. Within the matrix lithology of GRA 95209, the dominant opaque mineral is kamacite, which occurs as grains reaching 3 mm in length with minor associated

Table 1
Modal mineralogy (vol %) calculated by image analyses of mineral maps (Fig. 5) for the matrix, metal-rich sheet, and metal-poor region of GRA 95209 and average H chondrites from McSween et al. (1991)

Mineral	Matrix	Metal-rich	Metal-poor	Avg. H chondrite
Olivine	25.9	13.9	35.4	35.0
Orthopyroxene	25.4	8.5	25.3	26.2
Clinopyroxene	3.8	7.3	6.6	4.1
Feldspar	5.8	3.6	13.4	9.6
Kamacite	35.2	62.7	14.8	18.0
Troilite	0.5	0.2	2.3	5.5
Phosphates	1.5	1.3	2.3	0.7
Graphite	1.9	2.4	—	—
Ol/(Ol + Px)	50.5	61.9	58.3	57.3
Pl/Total Sil	9.6	10.8	16.6	12.8
Tr/(Tr + Metal)	1.4	0.4	13.5	23.3

troilite, schreibersite, tetrataenite, chromite, graphite, and phosphates. Kamacite is typically 6.0–6.5 wt% Ni. Kamacite–kamacite and kamacite–troilite grain boundaries sometimes contain grains of tetrataenite (up to 20 μm thick) and schreibersite (up to 65 μm thick). Schreibersite typically contains 50 wt% Ni and 14.6 wt% P. Kamacite and troilite also occur as veins up to 20 μm wide and several hundred micrometers long and in 1–5 μm diameter blebs within mafic silicates. These latter occurrences are typical of acapulcoites (Zipfel et al., 1995; McCoy et al., 1996). Graphite occurs within metal as rosettes up to 240 μm in diameter. Phosphates occur rimming metal grains, as stringers within metal grains and as distinct larger agglomerations of one or more phosphates. Similar petrographic occurrences were previously described by Floss (1999). Floss (1999) reported the occurrence of chladniite occurring with a second phosphate whose composition was intermediate between farringtonite and sarcopside/graftonite. We also observed chladniite ($Ca_{0.67}Na_{1.77}(Mg_{5.76}Fe_{1.16}Mn_{0.60})_{\Sigma=7.52}(PO_4)_6$) and farringtonite ($(Mg_{2.36–2.62}Fe_{0.60–0.40}Mn_{0.06–0.04}(PO_4)_2$) (Table 3).

The metal-poor region contains smaller kamacite grains, with most 0.5 mm or less in maximum dimension and the largest reaching 1 mm. Although the associated mineralogy is similar and includes troilite, tetrataenite, chromite, graphite, and phosphates, the abundance and occurrence of these phases differs substantially from the matrix lithology. Troilite and metal occur in veins and silicate-enclosed blebs, as described above. Troilite also occurs as distinct grains reaching a few hundred micrometers across. The distribution of troilite and metal is very heterogeneous and areas of 1–3 mm in diameter can vary in their troilite/metal ratio from nearly zero to one (Fig. 5). Kamacite contains ~5.6 wt% Ni, while the included tetrataenite is typically ~52 wt% Ni. Graphite is considerably more abundant than in the matrix lithology. While graphite rosettes can reach several hundred micrometers, they tend to occur as very small rosettes and upwards of a dozen graphite rosettes sometimes occur in a single metal grain (Fig. 6). Phosphates commonly occur as stringers within these same metal grains and sometimes occur as lamellae along the crystallographic

Table 2
Silicate compositions (in wt%) in the three lithologies of GRA 95209

Element	Matrix (PTS, 40)				Metal-rich (PTS, 150)				Metal-poor (PTS, 210)			
	Ol	Opx	Cpx	Plag	Ol	Opx	Cpx	Plag	Ol	Opx	Cpx	Plag
SiO_2	41.3(2)	57.8(2)	54.7(3)	62.8(4)	41.3(2)	57.6(2)	54.6(2)	62.9(4)	41.3(2)	57.6(3)	54.5(2)	62.9(2)
TiO_2	0.11(1)	0.28(2)	0.68(2)	0.15(1)	0.11(2)	0.28(2)	0.67(3)	0.16(1)	0.11(2)	0.29(1)	0.67(2)	0.16(2)
Al_2O_3	b.d.	0.51(4)	1.27(4)	22.9(1)	b.d.	0.50(4)	1.27(3)	22.7(3)	b.d.	0.50(3)	1.27(3)	22.4(2)
Cr_2O_3	b.d.	0.7(1)	1.42(1)	n.d.	b.d.	0.74(8)	1.45(8)	n.d.	b.d.	0.75(6)	1.48(8)	n.d.
FeO	7.0(2)	4.8(1)	2.2(2)	0.12(6)	7.1(2)	4.9(2)	2.2(2)	0.3(2)	7.1(2)	4.9(1)	2.1(1)	0.3(1)
MnO	0.49(7)	0.58(5)	0.35(5)	b.d.	0.52(4)	0.57(5)	0.33(6)	b.d.	0.48(5)	0.57(5)	0.33(6)	b.d.
MgO	50.2(3)	33.2(3)	18.1(2)	b.d.	50.4(2)	33.3(2)	18.2(1)	b.d.	50.5(2)	33.3(3)	18.2(2)	b.d.
CaO	b.d.	1.7(1)	20.2(2)	3.7(1)	b.d.	1.69(5)	20.2(2)	3.6(2)	b.d.	1.67(8)	20.1(1)	3.7(1)
Na_2O	b.d.	0.09(3)	0.79(6)	9.3(2)	b.d.	0.09(2)	0.79(4)	9.3(2)	b.d.	0.10(2)	0.79(3)	9.4(1)
K_2O	n.d.	n.d.	n.d.	0.30(7)	n.d.	n.d.	n.d.	0.4(1)	n.d.	n.d.	n.d.	0.34(5)
Total	99.10	99.66	99.71	99.27	99.43	99.67	99.71	99.36	99.49	99.68	99.44	99.20
N	11	14	15	6	13	20	7	4	9	15	14	5
Fa	7.3(2)				7.3(2)				7.3(2)			
Fs		7.2(1)	3.7(2)			7.3(2)	3.6(3)			7.4(1)	3.5(2)	
Wo		3.2(2)	42.9(4)			3.3(1)	42.8(3)			3.2(2)	42.7(3)	
An				17.7(6)				17.2(8)				17.4(2)
Or				1.7(4)				2.4(5)				1.9(3)

b.d., below typical detection limits of 0.06 wt% for Al_2O_3, Cr_2O_3, and K_2O and 0.04 wt% for MnO, MgO, and CaO; n.d., not determined; values in parentheses indicate 1σ variability in the last digit.

Table 3
Representative phosphate compositions (in wt%) for the three lithologies of GRA 95209

Element	Matrix (PTS, 40)			Metal-rich (PTS, 150)			Metal-poor (PTS, 210)	
	Chladniite	Farringtonite		Farringtonite	Graftonite/sarcopside	Chladniite	Whitlockite	Chladniite
FeO	10.6	10.5	15.3	12.4	45.5	14.3	3.53	6.74
MnO	5.15	0.80	1.47	0.67	13.5	7.70	b.d.	2.64
MgO	25.7	39.0	34.2	37.5	0.35	21.4	2.64	30.1
CaO	4.01	b.d.	b.d.	b.d.	b.d.	3.94	45.5	5.90
Na_2O	6.32	b.d.	b.d.	b.d.	b.d.	6.09	2.29	5.40
P_2O_5	48.1	51.9	50.8	51.4	40.7	47.3	45.3	49.9
Total	99.88	102.20	101.77	101.97	100.05	100.73	99.26	100.68

b.d., below typical detection limits of 0.06 wt% for Na_2O and 0.04 wt% for MnO and CaO.

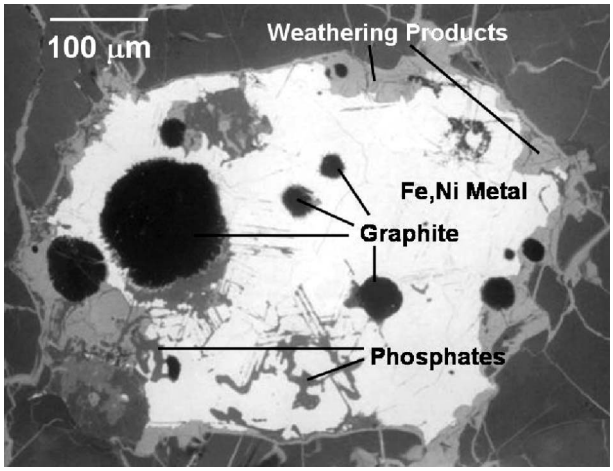

Fig. 6. Back-scattered electron image of a metal grain in the metal-poor lithology of GRA 95209 showing included graphite rosettes, stringers of phosphates (including some occurring along the crystallographic axes of the enclosing kamacite), and terrestrial weathering products.

axes of the kamacite. The phosphates in the metal-poor lithology are chladniite ($Ca_{0.88}Na_{1.48}(Mg_{6.26}Fe_{0.92}Mn_{0.36})_{\Sigma=7.52}(P_{0.99}O_4)_6$) and whitlockite ($Ca_{8.89}(Mg_{0.70}Fe_{0.56}\ Mn_{0.02})_{\Sigma=1.28}\ Na_{0.74}\ (P_{1.00}O_4)_7$) (Table 3).

The metal-rich sheet present in GRA 95209 differs in several significant ways from metal in the other two lithologies. Apart from being considerably more abundant, the metal vein is composed of kamacite grains with widths of ~0.5–1 mm and length/width ratios of $\geqslant 3$. Within the kamacite grains are abundant schreibersite grains. Elongate kamacite lamellae are composed of kamacite subgrains with minute (1–5 μm) schreibersites at the grain boundary, whereas interstitial kamacite regions contain larger (10–50 μm) which are often elongate and aligned with the axis of the interstices. Kamacite averages 6.2 wt% Ni, with associated schreibersite containing ~42 wt% Ni and ~14.7 wt% P. No tetrataenite was observed. Graphite rosettes within the metal sheet are not abundant, but do reach impressive sizes (up to 4 mm in

maximum dimension). Phosphates occur as stringers within and rimming kamacite. Mineralogically, they are similar to those in the matrix lithology, with chladniite ($Ca_{0.61}Na_{1.77}(Mg_{4.72}Fe_{1.82}Mn_{1.03})_{\Sigma=7.57}(P_{1.00}O_4)_6$) and Fe,Mg, Mn-phosphates ranging in composition between graftonite/sarcopside ($Fe_{2.24}Mg_{0.03}Mn_{0.67}(PO_4)_2$) and farringtonite ($Mg_{2.55}Fe_{0.47}Mn_{0.03}(PO_4)_2$) (Table 3). Interestingly, although mineralogically similar to phosphates in the matrix lithology, the phosphates associated with the metal-rich sheet are considerably richer in Fe and Mn. Where the metal sheet abuts the surface of the meteorite, remnants of the fusion crust are observed, although this zone is quite weathered, and a heat-altered α_2 zone extends to a depth of ~1 mm.

4. ^{39}Ar–^{40}Ar dating

To define the time of early metamorphism experienced by GRA 95209, we analyzed a sample using the ^{39}Ar–^{40}Ar dating technique. A 47.6 mg matrix sample of GRA 95209 was irradiated with fast neutrons to convert part of the ^{39}K to ^{39}Ar. The irradiation constant ($J = 0.02843 \pm 0.00005$) was determined from samples of the NL-25 hornblende (Bogard et al., 1995) irradiated along with GRA 95209. The J values for three NL-25 samples in each of two parallel irradiation tubes defined linear trends of identical slope, from which the J value for GRA 95209 was deduced from its relative irradiated position. Argon was extracted by stepwise heating and its isotopic composition was measured on a mass spectrometer. Small corrections were applied for blanks and reactor-produced interferences. ^{39}Ar–^{40}Ar ages were calculated for each extraction using the ^{40}K decay parameters recommended by Steiger and Jäger (1977), which are $\lambda(\beta^-) = 4.962 \times 10^{-10}/y$, λ(e-capture) $= 0.581 \times 10^{-10}/y$, and ^{40}K abundance $= 0.01167\%$.

The ^{39}Ar–^{40}Ar ages and K/Ca ratios plotted against cumulative release of ^{39}Ar for stepwise temperature extractions of GRA 95209 are shown in Fig. 7. The K and Ca concentrations for our sample were 350 ppm and 1.8%, respectively. Age uncertainties for individual extractions include only the uncertainty in the ^{40}Ar/^{39}Ar ratio after appropriate corrections. The total Ar–Ar age across all extractions is 4.508 Ga. Nine extractions releasing ~6–84% of the cumulative ^{39}Ar give constant Ar–Ar ages and K/Ca ratios. The average K/Ca ratio of 0.09 for these nine extractions is identical to that measured in matrix feldspar (Table 2). The average age for these nine extractions is 4.521 ± 0.006 Ga. The uncertainty in this age is derived from one sigma of the distribution of these nine ages about the mean, combined with the uncertainty in irradiation constant, J (Bogard et al., 2000). It does not include a $\leqslant$0.5% uncertainty in absolute age of the NL-25 hornblende monitor. An isochron plot of ^{40}Ar/^{36}Ar versus ^{39}Ar/^{36}Ar for these same extractions gives an age of 4.522 ± 0.005 Ga and a ^{40}Ar/^{36}Ar intercept within error of zero. The first few extractions releasing ~6% of the total ^{39}Ar show variable Ar–Ar ages and K/Ca ratios. Variable

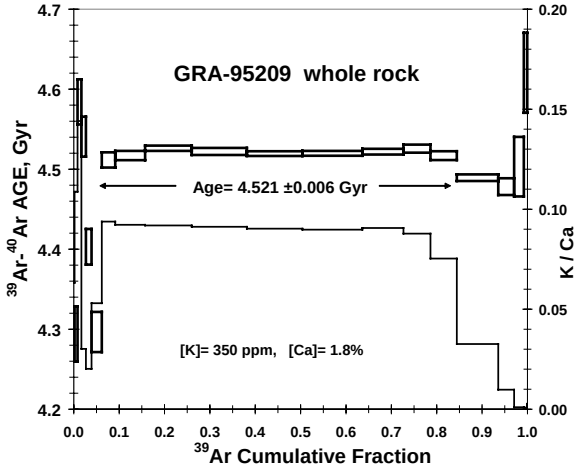

Fig. 7. ^{39}Ar–^{40}Ar ages (rectangles, left scale) and K/Ca ratios (stepped line, right scale) as a function of cumulative release of ^{39}Ar for stepwise temperature extractions of GRA 95209 matrix. Individual age uncertainties are indicated by the width of the rectangles and include all analytical uncertainties in the ^{40}Ar/^{39}Ar ratio.

K/Ca ratios at low temperatures are characteristic of many Antarctic meteorites and are thought to result from weathering and K redistribution on grain surfaces. We interpret the variable Ar ages in this region as resulting from diffusive loss of radiogenic ^{40}Ar and recoil loss of ^{39}Ar from K-enriched material on grain surfaces during neutron irradiation (e.g., Bogard and Garrison, 2003). Above ~84% cumulative ^{39}Ar release, the onset of degassing of Ar from pyroxene, having much lower K/Ca ratios, causes the K/Ca ratio to decrease. The Ar–Ar age also decreases slightly here, and we interpret the age decrease to have resulted from gain of recoiled ^{39}Ar onto surfaces of pyroxene grains. We conclude that the plateau age of 4.521 ± 0.006 Ga is a precise measure of the time of closure of the K–Ar system in GRA 95209.

The ^{36}Ar/^{38}Ar and ^{36}Ar/^{37}Ar ratios are relatively constant for those extractions defining the Ar–Ar age plateau, and the ^{36}Ar/^{38}Ar ratios are close to the expected cosmogenic value of ~0.7. However, for higher temperature extractions releasing Ar from pyroxene, both of these ratios increase substantially. We interpret these extractions to have released $\sim 1 \times 10^{-8}$ cm^3/g of trapped ^{36}Ar. This ^{36}Ar concentration is slightly higher than that reported for a metal-rich fraction of GRA95209 (Busemann and Eugster, 2002) and represents trapped Ar not degassed during lodranite metamorphism.

We previously reported ^{39}Ar–^{40}Ar ages for four acapulcoites (Acapulco, Monument Draw, ALH81187, and ALH81261) and the EET84302 transitional acapulcoite–lodranite to fall in the range 4.51–4.52 Ga (Mittlefehldt et al., 1996; McCoy et al., 1996). The weighted mean age of these five meteorites is 4.514 ± 0.004 and lies within uncertainties of the GRA95209 age of 4.521 ± 0.006 Ga reported here. An Ar–Ar age for Acapulco of 4.514 ± 0.016 Ga obtained by Pellas et al. (1997) is identical to the Acapulco age obtained at JSC

(4.510 ± 0.010 Ga). The Gibson lodranite (the only lodranite ^{39}Ar–^{40}Ar dated), however, yielded a distinctly younger age of 4.49 ± 0.01 Ga (McCoy et al., 1997a). (Because all Ar–Ar ages reported by JSC used the same NL-25 hornblende age monitor, the uncertainty in absolute age of NL-25 does not enter into relative comparisons of Ar–Ar ages.) It is noteworthy that the ages of GRA 95209 and EET 84302 (4.519 ± 0.017 Ga), which are so similar petrographically, are essentially identical, suggesting that they may have shared a common thermal history that was more similar to that of acapulcoites than lodranites.

Most meteorite parent bodies are thought to have formed prior to ~4.56 Ga ago (e.g., Carlson and Lugmair, 2000), but the Ar–Ar ages of acapulcoites are ~40 Ma younger than these likely formation times. McCoy et al. (1996) and Pellas et al. (1997) interpreted this difference as evidence for an extended metamorphic history of the acapulcoite–lodranite parent body, which caused the K–Ar chronometer to remain open for an extended period of time. Closure of the Ar–Ar chronometer in different acapulcoites occurred within a relatively narrow interval of time, which was much shorter compared to the metamorphism interval indicated for ordinary chondrites. Equilibrated ordinary chondrites show Ar–Ar ages ranging from ~4.52 Ga down to ~4.42 Ga (e.g., Turner et al., 1978) and Pb–Pb ages of ~4.56–4.50 Ga (Göpel et al., 1994), in spite of the observation that acapulcoites and lodranites were heated to higher metamorphic temperatures than were ordinary chondrites. The tight clustering of Ar–Ar ages for acapulcoites may indicate their derivation from the same region of the parent body. In possible support of this suggestion is the observation that space (CRE) exposure ages of most acapulcoites and lodranites fall in a narrow range (Herzog, 2003), likely indicating their ejection from the parent object in only a few impact events. In the cooling model presented for Acapulco by Pellas et al. (1997), initial cooling of the parent body was rapid down to temperatures of ~700 K, to account for the older Pb–Pb and I–Xe ages of 4.557 Ga (Brazzle et al., 1999), but was much slower for temperatures of <700K, in order to explain the younger Ar–Ar ages and even younger Pu fission track ages. By this model the segregation of Fe,Ni-FeS from silicate described above would have occurred prior to closure of the Ar–Ar age.

5. Graphite morphology and isotopic composition

A previous study of the Acapulco meteorite revealed a surprising level of heterogeneity in the carbon and nitrogen isotopic composition of graphite grains (El Goresy et al., 1995). Because of the presumed relationship between lodranites and acapulcoites, we decided to measure the isotopic composition of graphite grains in GRA 95209. Measurements were carried out in two series, both with a Cameca ims-6f ion microprobe. Initial examination of the graphites in the ion probe indicated very low N contents (measured as CN^-/C^- secondary ion ratios). Thus, to maximize the signal for N measurements, we first used a high primary Cs^+ current of ~20 nA and measured secondary ions of ^{12}C and ^{13}C with a Faraday cup ($^{12}C^-$ count rate $\sim 2 \times 10^8$ c/s) and $^{12}C^{14}N$ and $^{12}C^{15}N$ with an electron multiplier. A mass resolving power ($\Delta m/m$) of ~5000 was used, sufficient to resolve isobaric interferences. A terrestrial diamond of known C and N isotopic composition was used to correct measured isotopic ratios for instrumental fractionation and determine N contents. These conditions were used to analyze a large rosette in the metal-rich sheet and two smaller graphite grains in a single metal grain of the metal-poor lithology. These measurements revealed that the N contents were very low (~20–100 ppm, based on the CN^-/C^- sensitivity factor of Hoppe et al., 1995) and that the N present was isotopically normal within errors of ~10–15‰. Moreover, despite their being situated less than 100 μm apart in the same metal grain, the two small grains had $\delta^{13}C$ values that differed by 80‰, a difference as large or larger than the total range of C isotopic ratios previously measured in meteoritic carbon (excluding presolar grains).

Based on the initial results, for further measurements we decided to focus on C isotopes and use a different analytical procedure, namely the extreme energy filtering technique (Farquhar et al., 1999). In this method, high energy (350 eV) secondary ions are collected under low-mass-resolution conditions. The ^{12}CH interference on ^{13}C is suppressed by using high-energy ions and this technique has been shown to provide higher reproducibility $\delta^{13}C$ measurements than measurements using high mass resolution. A ~4 nA Cs^+ beam was focused to a few micrometers, yielding a ^{12}C secondary ion count rate of $\sim 8 \times 10^5$ c/s. A terrestrial graphite crystal was used to determine instrumental fractionation corrections. This second series of measurements confirmed the $\delta^{13}C$ values measured under high-mass-resolution conditions and yielded C isotope data for an additional 13 small graphite grains in the metal-poor lithology. The isotopic results are given in Table 4 and illustrated in Figs. 8 and 9.

The N contents of the GRA 95209 graphites are one to two orders of magnitude lower than those measured in Acapulco graphite by El Goresy et al. (1995). Also, whereas Acapulco graphites are isotopically light in N ($\delta^{15}N$ values = −160 to −60‰), the GRA95209 grains have N indistinguishable from terrestrial. We cannot rule out the possibility that the measured N is adsorbed terrestrial contamination. In any case, either the graphite grains were originally more N-rich, like those found in Acapulco, and thermal processing of GRA 95209 has led to N loss, or the grains formed with low N. We will discuss possible origins and histories of the graphite grains further below.

The distribution of measured $\delta^{13}C$ values for the GRA 95209 graphite grains is shown in Fig. 8. Several measurements of the large graphite rosette in the metal-rich sheet indicate an average $\delta^{13}C \sim -33‰$. The range of measured values (standard deviation ~5‰) is somewhat larger than

Table 4
Carbon and nitrogen isotopic compositions (‰) of graphite grains in GRA 95209

Sample	# meas.	$\delta^{13}C_{PDB} \pm 1\sigma$	$\delta^{15}N_{Air} \pm 1\sigma$	CN^-/C^-
Metal vein				
Large graphite	18	-33.4 ± 5.1	0 ± 11	2.6×10^{-4}
Metal-poor region				
G	4	44.8 ± 4.2	-8 ± 16	2.8×10^{-4}
H	6	-36.5 ± 1.7	3 ± 6	4.1×10^{-4}
I	4	81.0 ± 4.2	-14 ± 8	1.5×10^{-3}
J	2	80.6 ± 1.2	n.d.	n.d.
K	1	47.4 ± 5.5	n.d.	n.d.
L	1	-32.6 ± 5.1	n.d.	n.d.
M	1	30.4 ± 5.4	n.d.	n.d.
N	1	49.2 ± 5.5	n.d.	n.d.
O	1	47.1 ± 5.5	n.d.	n.d.
P	2	53.3 ± 1.3	n.d.	n.d.
Q	1	54.1 ± 5.5	n.d.	n.d.
R	1	48.4 ± 5.6	n.d.	n.d.
S	1	60.6 ± 5.6	n.d.	n.d.
T	1	67.3 ± 5.6	n.d.	n.d.
U	1	-49.0 ± 5.0	n.d.	n.d.

n.d., not determined.

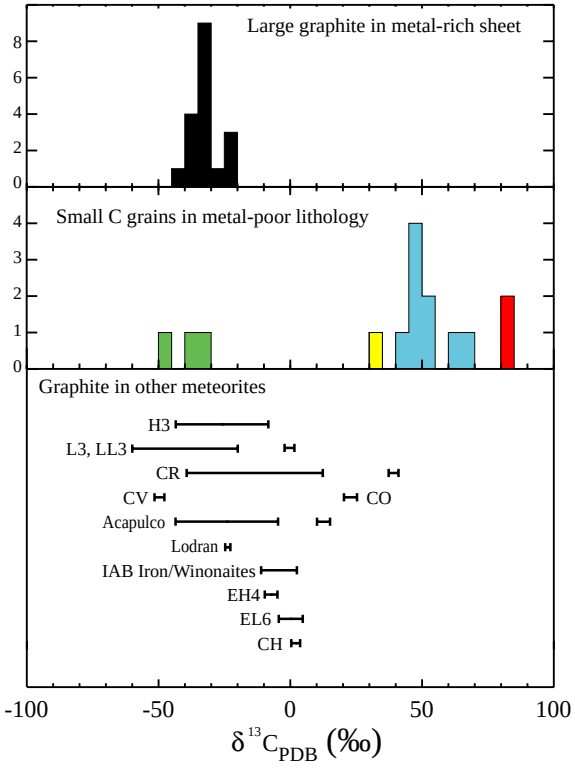

Fig. 8. C-isotopic compositions of graphite in GRA 95209 are compared with ranges observed for graphite in other meteorites. Data for EH, EL, and CH are from stepped combustion measurements of bulk samples (Grady et al., 1986; Grady and Pillinger, 1990). Other previous data are ranges of ion probe measurements in individual graphite grains (El Goresy et al., 1995; Mostefaoui et al., 1997, 2000; Zipfel et al., 1997).

would be expected from the measurement reproducibility of the standards, but there is no correlation between location within the grain and isotopic composition, and we thus attribute the spread in $\delta^{13}C$ values to analytical errors. In

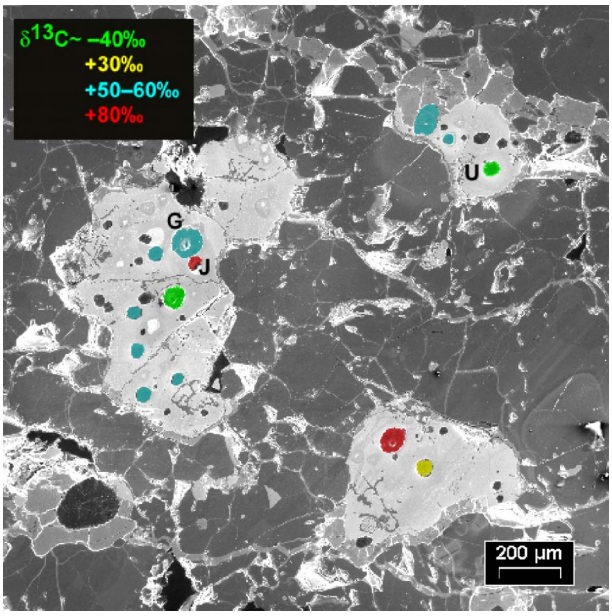

Fig. 9. Back-scattered electron image of metal grains in the metal-poor lithology of GRA 95209. Graphite rosettes are color-coded according to their C isotopic composition. Individual graphite grains within a single metal grain show a remarkable range of $\delta^{13}C$ values.

contrast, the small grains in the metal-poor lithology show a remarkable spread in C isotopic composition, with $\delta^{13}C$ ranging from $-50‰$ to $+80‰$, with the majority of grains having $\delta^{13}C > +30‰$. Even more striking is the observation of extreme isotopic heterogeneity even for graphites within single metal grains, illustrated in Fig. 8. The entire range of C isotopic ratios is seen for eight individual graphite grains within the single <1 mm metal grain shown on the left of Fig. 9.

Fig. 8 also compares the distribution of C isotopes in GRA 95209 with the ranges previously observed in graphite from several other meteorites classes. As in the present study, data for most of the plotted meteorite classes were obtained by ion probe measurements of individual grains, in most cases associated with metal. Data for EH, EL, and CH chondrites are from stepped combustion measurements of bulk samples. Although some of the GRA 95209 data, notably those of the large graphite rosette in the metal-rich sheet, overlap those of graphite in Acapulco and several other meteorite classes, it is clear that most of the small graphite grains are more ^{13}C rich than the vast majority of graphite measured in other meteorites.

Following the ion probe measurements, we extracted ultra-thin sections for transmission electron microscopy (TEM) studies of the graphite grains, from both the metal-poor lithology and the metal-rich sheet using focused ion beam (FIB) lift-out techniques (Stroud et al., 2000; Heaney et al., 2001). The TEM studies were performed with a Philips CM30 equipped with an Oxford Link EDS system. The FIB lift-out was performed with a FEI FIB 200 and an ex situ micro-manipulator equipped with a glass needle.

The graphite extracted from the metal-rich vein (Fig. 10A) is generally well crystallized, exhibiting a crystallite size of 100 nm to 1 μm and strong diffraction spots (Fig. 10B). Kamacite sub-grains (~20 nm) inside the graphite appear as dark spots in the TEM images and manifest as rings in the electron diffraction pattern. The Fe/Ni ratio (5 wt% Ni) of the kamacite sub-grains is comparable to that of the kamacite of the metal vein surrounding the graphite.

Sections of three different graphite rosettes (Fig. 9, grains G, J, and U) from two different metal grains in the metal-poor region were extracted. These grains have $\delta^{13}C$ values spanning the total range observed in the meteorite (Fig. 8). All three grains (Fig. 11A) are poorly crystallized, exhibiting annular diffraction patterns (Fig 11B), and little long-range order. The graphite in some cases forms a turbostratic rim, or mantle, around enclosed kamacite sub-grains. These kamacite grains are larger (150–250 nm) and lower in Ni concentration (1–3 wt%) than those contained in the metal-sheet-associated graphite. The irregular grain shape of the kamacites, contrast at the grain edges and rings in the diffraction patterns not indexed to kamacite, indicates pockets of interfacial carbide phase formation.

An ultra-thin section was also extracted from the metal surrounding graphite grain U. This metal showed 5–7 wt% Ni content, significantly higher than that found in the enclosed kamacite sub-grains.

6. Discussion

6.1. Similarity to other acapulcoites and lodranites

The silicate portion of GRA 95209 is strikingly similar to EET 84302. Both meteorites share a common texture, silicate mineralogy, silicate mineral compositions, lack of significant shock effects, and ^{39}Ar–^{40}Ar age (Mittlefehldt et al., 1996; McCoy et al., 1997a). Mittlefehldt et al. (1996) and McCoy et al. (1997a,b) argued that EET 84302 was transitional between the acapulcoites—which experienced Fe,Ni-FeS melting and melt migration without silicate melting—and lodranites—which experienced both Fe,Ni-FeS and silicate partial melting and melt migration. This description seems to fit for GRA 95209 as well and we invoke a similar origin to that championed for EET 84302. As we discuss next, GRA 95209 differs from EET 84302 and is remarkable because of the complex mineralogy and textures in its opaque components. It seems an inescapable conclusion that these features may be common on the acapulcoite–lodranite parent body. Although they are apparent in the large meteorite GRA 95209 (948.8 g

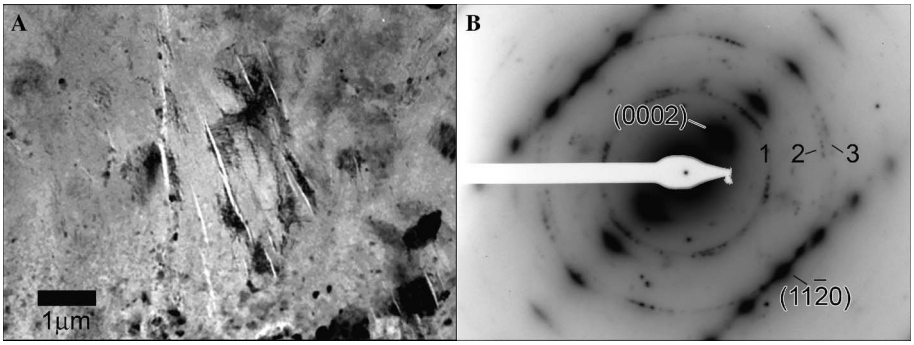

Fig. 10. Transmission electron microscopy of the graphite from the metal sheet region. The bright-field image (A) shows 1–100 nm nodules of kamacites in a matrix of well-graphitized carbon. The diffraction pattern (B) shows a [1–100] zone-axis pattern of graphite, overlayed with diffuse rings of the nanocrystalline kamacite. The labels correspond to: (1) (110), (2) (200), and (3) (211) spacings of kamacite.

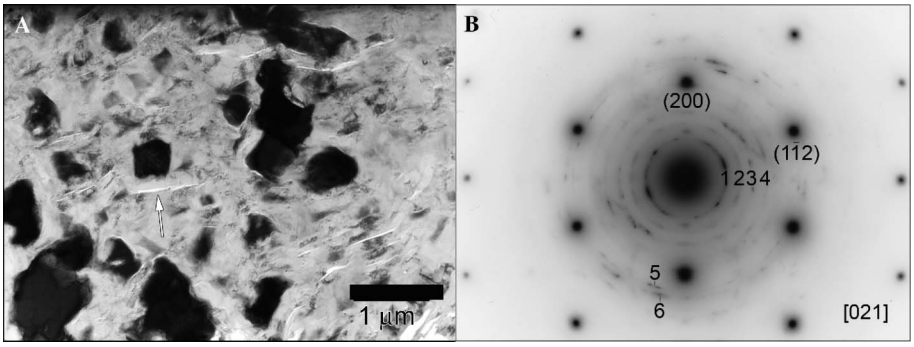

Fig. 11. Transmission electron microscopy of a section from graphite rosette U of Fig. 9. The bright-field image (A) shows 10–500 nm crystallites of kamacite in a poorly ordered matrix of graphite. The arrow indicates a region of graphite that forms a rim surrounding a kamacite grain, consistent with a Fischer–Tropsch type growth mechanism. The diffraction pattern (B) shows a [021] zone axis pattern of an interior kamacite grain overlayed with diffuse rings from graphite, and a possible interfacial carbide phase. The labels correspond to: (1) (0002) graphite, (2) 0.258 nm, interfacial phase, (3) (10–10) graphite, (4) (10–12) graphite, 5 (11–20) graphite, 6 (11–22) graphite.

main mass), they are not preserved in small meteorites like EET 84302 (59.59 g main mass).

6.2. Melting, melt migration, and geochemical consequences

The evidence for melting within GRA 95209 is unambiguous, although the extent of that melting is less clear. In particular, evidence for partial melting of silicates and subsequent melt migration is ambiguous. Mittlefehldt and Lindstrom (1998) reported Na/Sc, Sm/Sc, Sm/Yb, and Eu/Yb ratios for two splits. While lithophile element ratios typical of acapulcoites were measured for one split, the other exhibited acapulcoite-like Na/Sc and Eu/Yb ratios, but lodranite-like Sm/Sc and Sm/Yb ratios and REE patterns, suggestive of either removal of low-degree silicate partial melt or slight undersampling of phosphates. Modal analyses (Table 1) suggest plagioclase/total silicate ratios within the range of those expected for chondritic materials, suggesting that basaltic (pyroxene–plagioclase) partial melts have not been mobilized to any significant degree. Textural criteria are also ambiguous. GRA 95209 is coarser-grained than is typical for acapulcoites. McCoy et al. (1997a) suggested that this grain coarsening occurred in the presence of partial melts. Evidence for partial melting of a plagioclase-rich component was found in the intermediate EET 84320 in the form of plagioclase grains enveloping mafic silicates. Similar plagioclase morphologies are observed in GRA 95209, suggestive of low degrees of silicate partial melting. However, we also observe micron-scale Fe,Ni-FeS veins cross-cutting plagioclase, which McCoy et al. (1996) observed in acapulcoites and suggested that the plagioclase grain was solid at the time of Fe,Ni-FeS melting and remained solid throughout the history of the rock. Finally, some areas of GRA 95209 exhibit a seemingly preferential association of calcic pyroxene and plagioclase, as expected from crystallization of a low-degree silicate partial melt, although this association is not observed on a thin-section wide basis (Fig. 5). Thus, we suggest that silicate partial melting probably occurred locally and heterogeneously within GRA 95209 and the bulk peak temperature probably barely exceeded the silicate solidus (~1050 °C).

In strong contrast to the ambiguity over silicate partial melting, there can be no question that extensive Fe,Ni-FeS partial melting occurred and that migration of these melts produced the spectacular series of veins and dikes observed in GRA 95209. Metallic veins are known from acapulcoites, having been observed in the acapulcoite Monument Draw (McCoy et al., 1996). However, the CT scanning reported above provides the opportunity to examine these veins and dikes in three dimensions. In GRA 95209, metal migration occurred primarily within the large metal dike now sampled as the capping sheet on this flight-oriented stone. Volumetric analyses suggest that the metal-rich sheet occupies more than three times the volume of the metal-poor region. Thus, the metal-rich sheet could not have been derived from within the volume of the current GRA 95209 meteorite. Instead, it appears likely that the metal-rich sheet was intruded into the current GRA 95209 matrix from a source region perhaps far removed on the parent body. McCoy et al. (1997b) calculated that veins of molten metal–sulfide in the range of 1 mm to 1 cm wide migrating through a solid silicate matrix might reach lengths up to 1 km on asteroidal bodies where pressures would be negligible. Within GRA 95209, migration of Fe,Ni-FeS veins and dikes was more complicated than migration of a single, large dike. A complex network of branching and rejoining veins and dikes occurs, with widths from 1 mm to more than a cm. The smaller of these are often disconnected, perhaps either because their length exceeds that which can be supported by the fluid or because they closed intermittently as fluid was extracted. One consequence of this branching structure is that it greatly increases the surface area of contact between the migrating metal–sulfide melts and the silicate-dominated matrix, increasing the likelihood of chemical reaction between these two reservoirs. Other evidence of metal–sulfide melt migration is preserved in GRA 95209, although expressed in a more subtle form. The metal-poor region sharply contrasts with the dominant matrix lithology both because of its metal-poor nature and its abundant troilite, strongly suggesting that metal–sulfide melts probably migrated locally within GRA 95209, particularly in the area of the metal-poor region. It is possible that this particular region served as a feeder zone for a metal–sulfide vein not preserved within the main mass of GRA 95209.

The physical complexity of the metal–sulfide veins is exceeded by the chemical complexity of this system. Like the vein in Monument Draw, the metallic sheet in GRA 95209 is dominated by metallic Fe,Ni in proportions far in excess of that expected for an Fe,Ni-FeS cotectic melt (85 wt% FeS, 15 wt% Fe). We suggest that this does not reflect extensive melting of the metallic component in GRA 95209, with a melting temperature for pure iron of 1535 °C. If this temperature had been reached, we would expect to see extensive evidence for silicate partial melting and melt migration. Instead, the formation of the metallic sheet probably involved melting at the Fe,Ni-FeS cotectic temperature (~950 °C), followed by separation of the metal and sulfide components as a result of liquid immiscibility upon cooling and crystallization. The supposition that this vein formed at low temperature is supported by the abundance of C and P within the vein, as these elements are typically enriched in low-degree partial melts (e.g., Kracher, 1985).

The mineralogy of GRA 95209, particularly the opaque mineralogy associated with the metal–sulfide veins, is substantially more complex than observed in any previous acapulcoite or lodranite, testifying to what must have been a dynamic chemical environment of reaction, oxidation and reduction. It is difficult to assess fully the nature of these reactions, given their complexity. GRA 95209 exhibits mineralogical differences both between the lithologies and between the whole rock and slightly melted acapulcoites.

The two most substantial of these differences are in the phosphate assemblages and in the minerals included within metal. The complexity of the phosphates was first noted by Floss (1999), who suggested that graftonite/sarcopside and farringtonite formed by oxidation of P in metal and reaction with mafic silicates, while chladniite formed by reaction between the resulting Fe,Mg-phosphates and plagioclase (the carrier of Na and Ca). This model was supported by the near absence of rare earth elements in Fe,Mg-phosphates (Floss, 1999) and is consistent with our observation that Fe,Mg-phosphates in contact with the large metal sheet tend to be more Fe-rich than those in the matrix lithology. It has some difficulty, however, explaining the coexistence of whitlockite and chladniite in the metal-poor lithology, which was not studied by Floss (1999), in the absence of an intermediate Fe,Mg-phosphate phase, although these authors did note that formation of chladniite could have occurred directly by reaction between Ca-phosphate (whitlockite) and silicates.

While metal–silicate reactions likely played a key role in the formation of the diverse array of phosphates observed, oxidation–reduction reactions within the metal–sulfide phases also played a substantial role. A key observation supporting this contention is the difference in mineral assemblages between the metal-rich sheet and the matrix and metal-poor lithologies. Within the former, we observed an assemblage of kamacite + graphite + schreibersite, with no tetrataenite observed and phosphates occurring only at the edges of the metal-rich sheet. In contrast, the matrix contains kamacite + tetrataenite + phosphates + graphite, with rare schreibersite. These two mineral assemblages can be considered as an oxidation–reduction pair, with reaction between graphite and phosphates to produce reduced P in the metal, which upon cooling exsolves Ni-rich schreibersite, rather than the Ni-rich tetrataenite observed in the matrix and metal-poor lithology. If this model is correct, the concentration of graphite within the metal-rich sheet must have been higher initially, given that substantial amounts of graphite remain. One complexity in this scenario is that two lithologies in contact over a distance of millimeters apparently record quite different oxidation–reduction conditions. One explanation for this may be in the relative temperatures of the two lithologies. Given that melt migration distances for a cm-wide metal-rich sheet might approach hundreds of meters (McCoy et al., 1997b), it is quite possible that this sheet originated in a portion of the parent body several hundred degrees hotter than the surrounding matrix and reactions at those higher temperatures produced the reduction now observed within the metal-rich sheet. In contrast, the matrix lithology reached a lower peak temperature and reduction did not occur. This scenario is reminiscent of that observed by McCoy et al. (1997b) in LEW 86220, where a basaltic partial melt complementary to the residual lodranites with a temperature of perhaps 1200 °C intruded an acapulcoite host with a peak temperature of around 1000 °C. As we discuss, this difference in heating may have had profound effects on the morphology and isotopic composition of graphite included in metal.

A period of slow cooling and metamorphism is suggested by several lines of evidence. The 4.52 Ga argon closure age is consistent with a period of slow cooling lasting ~40 million years. The homogenization of silicates across all lithologies suggests a long period of solid-state equilibrium, particularly since the proposed phosphate-forming reactions might have had significant local impact on silicate compositions. Finally, the compositions of coexisting kamacite and schreibersite in the metal-rich sheet suggest equilibration at temperatures substantially below 450 °C (Clarke and Goldstein, 1978).

6.3. Origin and evolution of graphite

The isotope signatures, microstructures, and compositions of the graphites from the metal-rich and metal-poor lithologies reinforce the differences in thermal-processing histories. The uniform $\delta^{13}C$ values, large grain size, and high degree of crystallization of the metal-vein-associated graphite are consistent with high temperature processing. At a minimum, it is clear that the metal sheet reached temperatures high enough to equilibrate the Ni content of the kamacite sub-grains inside the graphite with the exterior metal sheet, i.e., ~1150 °C, the Fe-graphite eutectic point. In contrast, the large variation in $\delta^{13}C$ values, small graphite crystallite size, non-equilibrium grain shape, and low Ni content of the kamacite sub-grains from the graphite associated with metal-poor regions must reflect a more limited degree of thermal processing.

Most likely the large graphite rosettes in the metal sheet formed by coalescence of smaller preexisting graphite grains and/or by exsolution of dissolved C from the metal. If the former, the high temperatures caused the graphite to re-crystallize and isotopically homogenize. The average $\delta^{13}C$ value of the large graphite grain we measured is $\sim -33‰$, slightly lighter than the bulk value measured in both Acapulco and Lodran of $\sim -23‰$ (Grady et al., 1993), but within the range of individual graphite grains from Acapulco (El Goresy et al., 1995). However, it is significantly lower than most of the small graphites measured in the metal-poor lithology; the majority of these have $\delta^{13}C > +40‰$ (Fig. 8). Thus, if the large well-crystallized graphite grains were formed by accumulation of smaller grains, these must have been a different population than those we have analyzed in the metal-poor region. The isotopic similarity of the large graphite to bulk acapulcoite and lodranite C suggests that its $\delta^{13}C$ value is closer to the bulk value for GRA 95209, and that the isotopically heavy compositions of many of the small graphites in the metal-poor region might be less representative of the bulk parent body.

The origin of the graphite grains in the metal-poor lithology is much less clear, but we can get some clues from their microstructures and isotopic compositions. Formation of the graphites by precipitation exsolution is inconsis-

tent both with the microstructure, which shows poorly graphitized carbon organized around kamacite sub-grains that possess a distinct composition from the host metal, and with the existence of a wide range of $\delta^{13}C$ values for graphites within a single metal grain. The latter observation indicates that the individual grains formed separately and were incorporated into the metal grains when they were molten, either on the parent body during partial melting or in the solar nebula during a high-temperature event (e.g., chondrule formation).

The graphite rosettes resemble in many ways spherulitic carbon inclusions in metal of both unequilibrated ordinary chondrites (Mostefaoui et al., 2000) and Acapulco (El Goresy et al., 1995). As in the present work, both of these studies found a wide range of C isotopic compositions of the graphite inclusions, sometimes within a single metal grain. Mostefaoui et al. (2000) reported Raman analyses of the inclusions in both UOCs and Acapulco. The Raman spectra indicated that the carbon inclusions consist of poorly graphitized carbon, with a typical crystallite size (within graphite sheets) of <5 nm for UOCs and ~8–23 nm for Acapulco. The higher degree of crystallization in Acapulco was interpreted as reflecting the higher degree of thermal processing that meteorite has experienced, relative to the UOCs. Mostefaoui et al. (2000) proposed that the metal-associated carbon inclusions in the UOCs formed from organic matter in the solar nebula during chondrule-forming events. In this scenario, the observed isotopic heterogeneity reflects isotopic heterogeneity in the organic precursors.

Despite some similarities, there are key differences between the GRA 95209 graphites and those studied by Mostefaoui et al. (2000) and El Goresy et al. (2005). First, the GRA 95209 grains have much lower nitrogen contents than the grains studied in either Acapulco or in the UOCs. Second, the graphite crystallite size inferred here from TEM observations (10–100 nm) is larger than that inferred by Raman for the other meteorites. However, comparing results of Raman and TEM studies of carbonaceous matter is non-trivial (Wopenka and Pasteris, 1993). For example, the Raman technique is most sensitive to the size of aromatic domains within graphite sheets, but TEM will determine crystallite sizes both along graphite sheets and in the stacking direction. Moreover, the Raman studies would not reveal whether or not tiny Fe–Ni grains are enclosed in the carbonaceous material as is the case for the GRA 95209 samples. Unfortunately, an attempt to perform Raman measurements of the GRA 95209 graphites was unsuccessful due to severe polishing damage of the grain surfaces (M. Fries, pers. comm.). Third, although all three sample types display a wide range of C isotopic ratios, the $\delta^{13}C$ range observed here for the most part does not overlap the ranges observed in primitive chondrites or Acapulco (Fig. 8). Taken together, these differences imply that either the GRA 95209 graphites formed by different mechanisms than did the grains observed in other meteorites and/or they formed from different C-rich precursors. Moreover, the higher degree of crystallization observed here probably reflects the much higher degree of thermal processing that GRA 95209 has experienced, compared to UOCs and Acapulco.

At the nanoscale, the observed microstructures are similar to carbonaceous material observed by TEM both in interplanetary dust particles (IDPs, Fraundorf, 1981; Christoffersen and Buseck, 1983; Bradley et al., 1984; Bradley, 1994) and in some C-rich aggregates in unequilibrated ordinary chondrites (Brearley, 1990). Like those observations, the grains studied here consist of poorly crystallized graphite in intimate association with larger crystals of Fe–Ni metal, in some cases with evidence for carbide at metal–C interfaces. These microstructures match those formed by catalytic reaction of C-bearing gases such as CO on metal surfaces to produce hydrocarbons, elemental carbon, and carbides (e.g., Fischer–Tropsch-type or FTT processes, Hindermann et al., 1993; Llorca and Casanova, 1998) and this appears to have played a role in forming the structures observed both in IDPs and in ordinary chondrites (Bradley et al., 1984; Brearley, 1990; Llorca and Casanova, 1998). The similarity of the graphite grains in the metal-poor lithology of GRA 95209 to these other materials indicates that they most likely formed by a similar process. Note that the catalytic process proposed here is fundamentally different than that proposed by Mostefaoui et al. (2000) to explain the graphites found in ordinary chondrites. In the Mostefaoui et al. (2000) scenario, the precursor material to the graphite is organic matter heated to high temperatures during chondrule formation. In the FTT scenario, the precursor material to the poorly graphitized carbon is CO gas that is catalytically dissociated at metal grain surfaces. Thus, the differences in N abundance and C isotopic composition between the small UOC graphites and those observed in GRA95209 most likely reflect different precursors (N-rich organics versus CO).

If the small GRA 95209 graphites indeed formed by a FTT process, what is the origin of the CO that reacted with the Fe–Ni metal and why was it isotopically heterogeneous? Although the $\delta^{13}C$ values of some of the small metal-associated graphites in the metal-poor region are within the range of graphite in Acapulco and other meteorites (Fig. 8), the majority of the small graphite grains has $\delta^{13}C > +30‰$. This range is too large to be explained by isotopic fractionation processes from a single reservoir. The ^{13}C-rich compositions are much heavier than the vast majority of previous measurements of organic and elemental C in meteorites, excluding presolar grains, but are similar to those measured in carbonates of CI, CM, and CR carbonaceous chondrites (Grady and Wright, 2003). The heavy signature of the C chondrite carbonates is not well understood. Lancet and Anders (1970) originally suggested that the large isotopic difference between the carbonates ($\delta^{13}C > +40‰$) and organics ($\delta^{13}C < -10‰$) could be explained by formation of the organics by a FTT process and presented experiments demonstrating a C-isotope fractionation between hydrocarbons and CO_2 of the right

magnitude and direction during a FTT process. However, it is now widely accepted that the organics in chondrites have an interstellar heritage (Alexander et al., 1998) and did not form from FTT reactions of nebular CO. Moreover, FTT experiments by Yuen et al. (1990) under more realistic nebular conditions than those considered earlier (Lancet and Anders, 1970) indicated much more limited isotopic fractionations, though still in the direction that oxidized C is heavier than reduced C. It is now believed that the carbonates in carbonaceous chondrites formed by precipitation during aqueous alteration on the meteorites' parent asteroids. Thus, their C was most likely derived from material indigenous to the parents, with the heavy signature perhaps reflecting some contribution of C from highly anomalous presolar grains or from some as-yet-unrecognized ^{13}C-rich organic component.

Based on the above considerations, we consider two overall scenarios for the origin of the graphites: (1) in the parent asteroid or (2) in the solar nebula. If the graphites formed in the parent asteroid, a source of CO could be from reactions during planetary metamorphism (Sugiura et al., 1986; Brearley, 1990). In this case, isotopically light CO might form from reactions involving organics and isotopically heavy CO from thermal decomposition of carbonates, assuming that the parent body underwent aqueous processes such that carbonates formed similar to those found in carbonaceous chondrites. As the CO outgased from the planetary interior, it could encounter Fe–Ni metal and react to form elemental carbon and/or hydrocarbons. Small aggregates of these could then be absorbed into larger molten Fe–Ni grains during the partial melting inferred to have occurred in GRA 95209. The range of isotopic compositions would probably indicate several generations of degassing events. Although this scenario can in principle explain the range of isotopic compositions and microstructures observed in the carbon grains, it has some significant problems. First, there is no evidence that the parent body of the acapulcoites and lodranites was extensively aqueously altered as required to invoke carbonates like those found in CI, CM or CR chondrites. For example, the acapulcoites and lodranites are metal-rich, whereas the carbonate-bearing carbonaceous chondrites have very little metal. However, O isotopic compositions of acapulcoites and lodranites are more similar to carbonaceous chondrites than to other chondrite groups (Clayton and Mayeda, 1996, 1999) and the large range in O isotopes among these meteorites indicates that the parent body is quite heterogeneous. Second, the graphite rosettes are only found in GRA95209 within metal grains, but if the carbonaceous grains formed outside the metal grains and were subsequently absorbed by them, one might expect to also find some distributed within the silicates. Finally, although the metal-poor region of GRA95209 has clearly seen some melting and loss of melt compared to the matrix, the amount of melt migration in this lithology appears to be limited. Even if the metal grains hosting the isotopically heterogeneous graphites were molten, it is unlikely that they moved significant distances within the host rock. Thus, it is not clear how they would absorb such a diversity of graphite grains and why these would be somewhat homogeneously distributed throughout the metal grains.

If instead the graphite grains formed by a FTT process in the solar nebula prior to accretion of the lodranite parent body, the source of CO was most likely nebular CO itself. The isotopic composition of nebular CO is unknown, but as a dominant reservoir of C was probably close to the bulk solar system composition. The solar C isotopic composition is still uncertain, but measurements of lunar samples (Hashizume et al., 2004) indicate that it is in fact isotopically light ($\delta^{13}C < -100‰$), rather than ^{13}C rich as needed to explain the GRA95209 graphites. However, locally in the nebula, isotopic fractionation processes could lead to ^{13}C-rich CO. For example, during FTT synthesis of organics on metal grain surfaces, the reacting CO gradually becomes ^{13}C rich as ^{12}C gets transferred to reduced C phases (Yuen et al., 1990). However, assuming a starting composition similar to most meteoritic organic matter ($\delta^{13}C \sim -20‰$), reaching the very heavy compositions reported here would likely require unrealistically extensive processing of a large fraction of the nebular CO at high temperatures (Yuen et al., 1990). Thus, a nebular formation for the ^{13}C-rich graphites would probably require a ^{13}C-rich precursor, not yet identified in the meteoritic record, but perhaps related to the origin of the ^{13}C-rich carbonates in carbonaceous chondrites. In any case, the range of isotopic compositions would require either a large range of carbonaceous precursors or a large range in the extent of isotopic fractionations.

In the nebular scenario, following FTT formation of the carbonaceous material, the carbon-rimmed kamacites were incorporated into a larger, compositionally distinct Fe–Ni metal reservoir at low enough temperature to partially preserve the carbon rims, but high enough for partial graphitization. This incorporation could have taken place during heating events in the solar nebula (e.g., chondrule formation) or during or subsequent to accretion of the GRA 95209 parent body. The surrounding metal subsequently isolated the interior graphites from each other and from oxidation reactions, and thus preserved the isotopic heterogeneity established in the nebula. Thermal processing on the parent body could also have further graphitized the carbon beyond what is seen in metal-associated carbon in Acapulco.

7. Conclusions

GRA 95209 may provide our best opportunity to date to understand the earliest stages of core formation in asteroidal bodies. The texture, mineralogy, and mineral compositions within the metal and sulfide of this meteorite testify to a complex history of metal–sulfide melting, melt migration perhaps hundreds of meters into regions of differing thermal histories, reaction between the migrating melts and enclosing solids, and oxidation–reduction reactions as a function of vein composition and temperature. Perhaps the most star-

tling observation is the preservation of apparent nebular carbon isotopic compositions and structures in a rock that approached melting at the silicate solidus. This work suggests that carbon incorporated from the solar nebula into a differentiating asteroid or planet may be preferentially incorporated into early metal–sulfide melts that would ultimately form a core, but may not achieve isotopic homogeneity until extensive thermal processing occurs. The implications for this finding on the carbon budget for the Earth, and its biosphere, are topics of ongoing research.

Acknowledgments

We are grateful to R. Ketcham for assistance in obtaining the CT imagery; to C. Denison for CT image processing; to R. Schneider and A. Barnett for CT image analysis; and to L. Collins for X-ray mapping of the GRA thin sections. The detailed comments of the A.E. and two anonymous reviewers improved and clarified the manuscript. The high-resolution X-ray computed tomography facility at the University of Texas at Austin is supported by NSF Grant EAR-0345710; funding for CT scanning was provided by NSF Grant EAR-9902682. The petrology, argon analyses, and work on carbon morphology and isotopic composition were supported by the NASA Cosmochemistry Program.

Associate editor: Christian Koeberl

References

Alexander, C.M.O.D., Russell, S.S., Arden, J.W., Ash, R.D., Grady, M.M., Pillinger, C.T., 1998. The origin of chondritic macromolecular organic matter: a carbon and nitrogen isotope study. *Meteorit. Planet. Sci.* **33**, 603–622.

Bogard, D.D., Garrison, D.H., 2003. ^{39}Ar–^{40}Ar ages of eucrites and thermal history of asteroid 4 Vesta. *Meteorit. Planet. Sci.* **38**, 669–710.

Bogard, D.D., Garrison, D.H., Norman, M., Scott, E.R.D., Keil, K., 1995. ^{39}Ar–^{40}Ar age and petrology of Chico: large-scale impact melting of the L chondrite parent body. *Geochim. Cosmochim. Acta* **59**, 1383–1400.

Bogard, D.D., Garrison, D.H., McCoy, T.J., 2000. Chronology and petrology of silicates from IIE iron meteorites: evidence of a complex parent body evolution. *Geochim. Cosmochim. Acta* **64**, 2133–2154.

Bradley, J.P., 1994. Nanometer-scale mineralogy and petrography of fine-grained aggregates in anhydrous interplanetary dust particles. *Geochim. Cosmochim. Acta* **58**, 2123–2134.

Bradley, J.P., Brownlee, D.E., Fraundorf, P., 1984. Carbon compounds in interplanetary dust: evidence for formation by heterogeneous catalysis. *Science* **223**, 56–58.

Brearley, A.J., 1990. Carbon-rich aggregates in type 3 ordinary chondrites: characterization, origins, and thermal history. *Geochim. Cosmochim. Acta* **54**, 831–850.

Brazzle, R.H., Pravdivtseva, O.V., Meshik, A.P., Hohenberg, C.M., 1999. Verification and interpretation of the I–Xe chronometer. *Geochim. Cosmochim. Acta* **63**, 739–760.

Busemann, H., Eugster, O., 2002. The trapped noble gas component in achondrites. *Meteorit. Planet. Sci.* **37**, 1865–1892.

Carlson, R.W., Lugmair, G.W., 2000. Timescales of planetesimal formation and differentiation based on extinct and extant radioisotopes. In: Canup, R., Righter, K. (Eds.), *Origin of the Earth and Moon*. University of Arizona Press, pp. 25–44.

Christoffersen, R., Buseck, P., 1983. Epsilon carbide: a low temperature component of interplanetary dust particles. *Science* **222**, 1327–1328.

Clarke Jr., R.S., Goldstein, J.I., 1978. Schreibersite growth and its influence on the metallography of coarse-structured iron meteorites. In: *Smithsonian Contributions to Earth Science*, vol. 21.

Clayton, R.N., Mayeda, T.K., 1996. Oyxgen isotope studies of achondrites. *Geochim. Cosmochim. Acta* **60**, 1999–2017.

Clayton, R.N., Mayeda, T.K., 1999. Oyxgen isotope studies of carbonaceous chondrites. *Geochim. Cosmochim. Acta* **63**, 2089–2104.

El Goresy, A., Zinner, E., Marti, K., 1995. Survival of isotopically heterogeneous graphite in a differentiated meteorite. *Nature* **373**, 496.

El Goresy, A., Zinner, E., Pellas, P., Caillet, C., 2005. A menagerie of graphite morphologies in the Acapulco meteorite with diverse carbon and nitrogen isotopic signatures: implications for the evolution history of acapulcoite meteorites. *Geochim. Cosmochim. Acta* **69**, 4535–4556.

Farquhar, J., Hauri, E., Wang, J., 1999. New insights into carbon fluid chemistry and graphite precipitation: SIMS analysis of granulite facies graphite from Ponmudi, South India. *Earth Planet. Sci. Lett.* **171**, 607–621.

Floss, C., 1999. Fe,Mg,Mn-bearing phosphates in the GRA 95209 meteorite: occurrences and mineral chemistry. *Am. Mineral.* **84**, 1354–1359.

Fraundorf, P., 1981. Interplanetary dust in the transmission electron microscope: diverse materials from the early solar system. *Geochim. Cosmochim. Acta* **45**, 915–943.

Göpel, C., Manhès, G., Allègre, C.J., 1994. U–Pb systematics of phosphates from equilibrated ordinary chondrites. *Earth Planet. Sci. Lett.* **121**, 153–171.

Grady, M.M., Franchi, I.A., Pillinger, C.T., 1993. Carbon and nitrogen chemistry of lodranites: relationship to Acapulco? *Meteoritics* **28**, 355 (abstract).

Grady, M.M., Pillinger, C.T., 1990. ALH85085: nitrogen isotope analysis of a highly unusual primitive chondrite. *Earth Planet. Sci. Lett.* **97**, 29–40.

Grady, M.M., Wright, I.P., 2003. Elemental and isotopic abundances of carbon and nitrogen in meteorites. *Space Sci. Rev.* **106**, 231–248.

Grady, M.M., Wright, I.P., Carr, L.P., Pillinger, C.T., 1986. Compositional differences in enstatite chondrites based on carbon and nitrogen stable isotope measurements. *Geochim. Cosmochim. Acta* **50**, 2799–2813.

Hashizume, K., Chaussidon, M., Marty, B., Terada, K., 2004. Protosolar carbon isotopic composition: implications for the origin of meteoritic organics. *Astrophys. J.* **600**, 480–484.

Heaney, P.J., Vicenzi, E.P., Giannuzzi, L.A., Livi, K.J.T., 2001. Focused ion beam milling; a method of site-specific sample extraction for microanalysis of Earth and planetary materials. *Am. Mineral.* **86**, 1094–1099.

Herzog, G., 2003. Cosmic-ray exposure ages of meteorites. In: Davis, A.M. (Ed.), *Meteorites, Comets, and Planets*. In: Holland, H.D., Turekian, K.K. (Eds.), *Treatise on Geochemistry*, vol. 1. Elsevier–Pergamon, Oxford, pp. 347–380.

Hindermann, J.P., Hutschings, G.J., Kiennemann, A., 1993. Mechanistic aspects of the formation of hydrocarbons and alcohols from CO hydrogenation. *Catal. Rev. Sci. Eng.* **35**, 1–127.

Hoppe, P., Amari, S., Zinner, E., Lewis, R.S., 1995. Isotopic compositions of C, N, O, Mg and Si, trace element abundances, and morphologies of single circumstellar graphite grains in four density fractions from the Murchison meteorite. *Geochim. Cosmochim. Acta* **59**, 4029–4056.

Ketcham, R.A., Carlson, W.D., 2001. Acquisition, optimization and interpretation of X-ray computed tomographic imagery: applications to the geosciences. *Comput. Geosci.* **27**, 381–400.

Kracher, A., 1985. The evolution of partially differentiated planetesimals: evidence from iron meteorite groups IAB and IIICD. In: *Proceedings of the 15th Lunar Planetary Science Conference. J. Geophys. Res.* **90**, C689–C698.

Lancet, M.S., Anders, E., 1970. Carbon isotope fractionation in the Fischer–Tropsch synthesis and in meteorites. *Science* **170**, 980–982.

Llorca, J., Casanova, I., 1998. Formation of carbides and hydrocarbons in chondritic interplanetary dust particles: a laboratory study. *Meteorit. Planet. Sci.* **33**, 243–251.

McBride, K., Mason, B., 1997. GRA 95209: Macroscopic and thin section description. *Antarct. Meteorite Newsl.* **20** (No. 1), 9.

McBride, K., McCoy, T., 1997. Revised hand sample description of GRA 95209. *Antarct. Meteorite Newsl.* **20** (No. 2), 9.

McCoy, T.J., Keil, K., Clayton, R.N., Mayeda, T.K., Bogard, D.D., Garrison, D.H., Huss, G.R., Hutcheon, I.D., Wieler, R., 1996. A petrologic, chemical and isotopic study of Monument Draw and comparison with other acapulcoites: evidence for formation by incipient partial melting. *Geochim. Cosmochim. Acta* **60**, 2681–2708.

McCoy, T.J., Keil, K., Clayton, R.N., Mayeda, T.K., Bogard, D.D., Garrison, D.H., Wieler, R., 1997a. A petrologic and isotopic study of lodranites: evidence for early formation as partial melt residues from heterogeneous precursors. *Geochim. Cosmochim. Acta* **61**, 623–637.

McCoy, T.J., Keil, K., Muenow, D.W., Wilson, L., 1997b. Partial melting and melt migration in the acapulcoite–lodranite parent body. *Geochim. Cosmochim. Acta* **61**, 639–650.

McSween Jr., H.Y., Bennett III, M.E., Jarosewich, E., 1991. The mineralogy of ordinary chondrites and implications for asteroid spectrophotometry. *Icarus* **90**, 107–116.

Meibom, A., Clark, B.E., 1999. Evidence for the insignificance of ordinary chondritic material in the asteroid belt. *Meteorit. Planet. Sci.* **34**, 7–24.

Mittlefehldt, D.W., Lindstrom, M.M., Bogard, D.D., Garrison, D.H., Field, S.W., 1996. Acapulco- and Lodran-like achondrites: petrology, geochemistry, chronology, and origin. *Geochim. Cosmochim. Acta* **60**, 867–882.

Mittlefehldt, D.W., Lindstrom, M.M., 1998. Petrology and geochemistry of lodranites Graves Nunataks 95209. *Meteorit. Planet. Sci.* **33**, A111.

Mittlefehldt, D.W., McCoy, T.J., Goodrich, C.A., Kracher, A., 1998. Non-chondritic meteorites from asteroidal bodies. In: Papike, J.J. (Ed.), *Planetary Materials. Rev. Mineral.* **36**, 4-1-195.

Mostefaoui, S., Perron, C., Zinner, E., Sagon, G., 2000. Metal-associated carbon in primitive chondrites: structure, isotopic composition, and origin. *Geochim. Cosmochim. Acta* **64**, 1945–1964.

Mostefaoui, S., Zinner, E., Hoppe, P., El Goresy, A., 1997. In situ survey of graphite in unequilibrated chondrites - Morphologies, C, N, and H isotopes. *Lunar Planet. Sci.* **XXVIII**, 989 (abstract).

Pellas, P., Fièni, C., Treiloff, M., Jessberger, E.K., 1997. The cooling history of the Acapulco meteorite as recorded by the ^{244}Pu and ^{40}Ar–^{39}Ar chronometers. *Geochim. Cosmochim. Acta* **61**, 3477–3501.

Rushmer, T., Minarik, W.G., Taylor, G.J., 2000. Physical processes of core formation. In: Canup, R.M., Righter, K. (Eds.), *Origin of the Earth and Moon*. University of Arizona Press, pp. 227–243.

Steiger, R., Jäger, E., 1977. Subcommission on geochronology: convention on the use of decay constants in geo- and cosmochronology. *Earth Planet. Sci. Lett.* **36**, 359–362.

Stöffler, D., Keil, K., Scott, E.R.D., 1991. Shock metamorphism of ordinary chondrites. *Geochim. Cosmochim. Acta* **55**, 3845–3867.

Stroud, R.M., Alexander, C.M.O'D., MacPherson, G.J., 2000. A precise new method of microsampling chondritic material for transmission electron microscope analysis: preliminary application to calcium–aluminum-rich inclusions and associated matrix material in the Vigarano CV3 meteorite. *Meteorit. Planet. Sci.* **35**, A153–A154.

Sugiura, N., Arkani-Hamed, J., Strangway, D.W., 1986. Possible transport of carbon in meteorite parent bodies. *Earth Planet. Sci. Lett.* **78** (2–3), 148–156.

Turner, G., Enright, M.C., Cadogan, P.H., 1978. The early history of chondrite parent bodies inferred from ^{40}Ar–^{39}Ar ages. In: *Proceedings of the 9th Lunar Planetary Science Conference*, pp. 989–1025.

Wasson, J.T., 1995. Sampling the asteroid belt: how biases make it difficult to establish meteorite-asteroid connections (abstract). *Meteoritics* **30**, 595.

Wopenka, B., Pasteris, J.D., 1993. Structural characterization of kerogens to granulite-facies graphite: applicability of Raman microprobe spectroscopy. *Am. Mineral.* **78**, 533–557.

Yuen, G.U., Pecore, J.A., Kerridge, J.F., Pinnavaia, T.J., Rightor, E.G., Flores, J., Wedeking, K., Mariner, R., Des Marais, D.J., Chang, S., 1990. Carbon isotopic fractionation in Fischer–Tropsch type reactions. *Lunar Planet. Sci.* **XXI**, 1367–1368 (abstract).

Zipfel, J., Palme, H., Kennedy, A.K., Hutcheon, I.D., 1995. Chemical composition and origin of the Acapulco meteorite. *Geochim. Cosmochim. Acta* **59**, 3607–3627.

Zipfel, J., Hutcheon, I.D., Marti, K., 1997. Carbon isotopic composition of graphite grains in the EL Taco IAB iron meteorite. *Lunar Planet. Sci.* **XXVIII**, 1627 (abstract).